ACS APPLIED MATERIALS & INTERFACES

www.acsami.org

Research Article

Cathode Interface Compatibility of Amorphous $LiMn_2O_4$ (LMO) and $Li_7La_3Zr_2O_{12}$ (LLZO) Characterized with Thin-Film Solid-State Electrochemical Cells

Alexander A. Delluva, Jessica Dudoff, Glenn Teeter, and Adam Holewinski*

Cite This: *ACS Appl. Mater. Interfaces* 2020, 12, 24992−24999

Read Online

ACCESS | Metrics & More | Article Recommendations | Supporting Information

ABSTRACT: Solid-state lithium-ion batteries are a hopeful successor to traditional Li-ion cells that use liquid electrolytes. While a growing body of work has characterized the interfaces between various solid electrolytes and the lithium metal, interfaces with common cathode intercalation compounds are comparatively less understood. In this contribution, the influence of polarization and temperature on interfacial stability between $LiMn_2O_4$ (LMO) and $Li_7La_3Zr_2O_{12}$ (LLZO) are investigated. Sputtered thin-film LMO electrodes are utilized to permit high-capacity cycling while retaining a large ratio of interfacial area to electrode bulk. Electrochemical impedance spectroscopy (EIS) is compared across a set of full (LMO|LLZO|Li) and symmetric (LMO|LLZO|LMO, Li|LLZO|Li, and Au|LLZO|Au) cells to delineate impedance features that are specific to the evolution of the cathode interface. Additional X-ray photoelectron spectroscopy (XPS) provides evidence of a limited interfacial reaction between LMO and LLZO that coincides with an increase in the impedance of the LMO−LLZO interface.

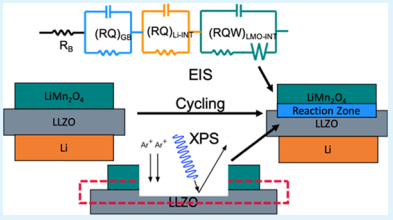

KEYWORDS: *solid-state electrolyte, lithium-ion battery, cathodic interface, impedance spectroscopy, garnet electrolyte, manganese spinel, solid interface*

INTRODUCTION

Lithium batteries utilizing solid-state electrolytes (SSEs) pose significant advantages over state-of-the-art Li-ion batteries, in terms of both safety and energy density. SSEs remove the need for flammable liquid electrolytes and associated safeguards, and they additionally hold the promise of enabling the use of lithium metal anodes. However, solid-state lithium batteries have not yet become widely commercially viable, with bulk conductivity and interfacial stability and impedance being primary hurdles.[1] Variables such as lattice mismatch, space charge distribution, and material interdiffusion or reaction can all play a role at both the cathode and anode SSE interfaces,[2] and a greater understanding of the interplay between these phenomena is necessary to advance solid-state battery technology.

Among lithium-conductive SSEs, $Li_7La_3Zr_2O_{12}$ (LLZO) has received much focus due to its good ionic conductivity ($\sim 10^{-4}$−10^{-3} S/cm) and stability in contact with the lithium metal over a wide voltage window (~0−5 V).[3−6] A growing body of research has characterized aspects of the anode (Li-metal) interface, addressing sources of impedance, overall stability, and dendritic growths.[6−8] Single crystal and neutron scattering studies have revealed that dendrites can still form in the absence of grain boundaries and that contributions from electronic conductivity in LLZO may be a factor in their formation.[9−11] Nonetheless, lithium stripping and plating at this interface has been demonstrated without dendritic short-circuiting at current densities greater than 1 mA/cm^2 (one proposed threshold for a commercial solid-state battery),[12,13] and Li−LLZO interfacial impedances of nearly 0 Ω have been achieved.[14] While there is still room for greater clarification, these studies highlight an increasingly firm understanding of the anodic LLZO interface. In contrast, the interface and compatibility of LLZO with various possible cathode insertion compounds has been investigated less extensively. One recent thermodynamic study has suggested that among a number of insertion compounds ($LiMn_2O_4$ (LMO), $LiFePO_4$ (LFP), $LiCoO_2$ (LCO), and $Li_4Ti_5O_{12}$ (LTO)), LMO may be the most stable against LLZO at room temperature (RT).[15] Another study evaluated the electrochemical stability of $LiMnO_2$, LFP, and LCO with first-principles calculations and suggested LCO to have the lowest electrochemical driving force for interfacial decomposition.[16] This corroborates a recent experimental study of the thermal stability of these three insertion electrodes, in which LCO tolerated the highest sintering temperature before interface decomposition phases were detected; however, no polarization conditions were explored.[17,18] Several electrochemical studies have probed LCO specifically,[19−22] including a detailed investigation by Vardar et al. using an array of synchrotron X-ray and other

Received: February 23, 2020
Accepted: May 5, 2020
Published: May 5, 2020

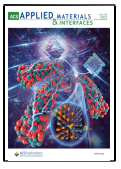

https://dx.doi.org/10.1021/acsami.0c03519
ACS Appl. Mater. Interfaces 2020, 12, 24992−24999

interface-sensitive techniques to identify decomposition products between LCO and LLZO.[23] Studies of LFP cycling have shown limited capacity fade over 100 cycles but without postcycling chemical characterization.[24] In contrast, the high-voltage cathode $LiMn_{1.5}Ni_{0.5}O_4$ was reported to be uncyclable with LLZO as the electrolyte,[25] while variations of nickel−cobalt−manganese cathodes showed interfacial degradation due to both cosintering[26] and electrochemical cycling.[27] The LMO−LLZO interface has been relatively unexplored, with only one study experimentally assessing the material's electrochemical operation over three cycles.[28] Thus, with a few exceptions, most cathodic interface studies to date have not taken the approach of combining electroanalytical techniques with interfacial chemical characterization to understand the effect of cycling.

For comparison, thin-film LMO cathodes have been more extensively explored with other electrolyte systems. These cathodes have shown excellent cycling performance in aprotic liquid electrolytes, as well the ability to be cycled at rates of 50C and upward.[29,30] More closely related to this study, LiPON-based all-solid-state batteries have shown a wide cycling window, and nanocrystalline LMO films (of the form $Li_xMn_{2-y}O_4$) have been stably cycled upward of 2000 times.[31] When utilizing the full voltage range available to these cells, capacities on the order of 270 mAh/g (LMO basis) have been observed.[32] Investigations into the charge-transfer reaction at LMO|LiPON found that the interface not only has good stability but also higher resistance than that of similar LCO−LiPON cells.[33]

In this contribution, we investigate the LMO−LLZO interface using sputtered thin-film LMO electrodes (i) to permit full-capacity cycling of a system with a high ratio of interface area to bulk volume, (ii) to remove the need for conductive additives and binders to probe only LMO−LLZO electrochemical interactions, and (iii) to facilitate access to the interface through ion milling.[18] We compare electrochemical impedance spectroscopy (EIS) of full cells (LMO|LLZO|Li) to symmetric cells (LMO|LLZO|LMO, Au|LLZO|Au, and Li|LLZO|Li) (Figure 1A−D) to delineate impedance features that

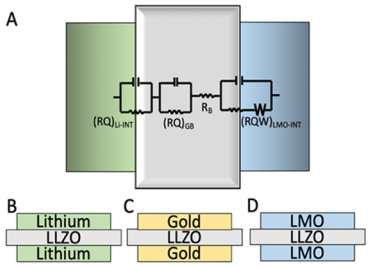

Figure 1. Cell architectures utilized for this study: (A) LMO|LLZO|Li, (B) Li|LLZO|Li, (C) Au|LLZO|Au, and (D) LMO|LLZO|LMO. The EIS equivalent circuit model ultimately determined is overlaid on the full cell (A).

are specific to the evolution of the cathode interface. The interface is probed by EIS at two operating temperatures and further characterized before and after cycling using X-ray photoelectron spectroscopy (XPS) depth profiling. We provide evidence of a limited interfacial reaction between LMO and LLZO at 100 °C, which corresponds with an increase in the equivalent circuit resistance of the LMO−LLZO interface as well as a capacity fade of ∼30% during the initial cycling of full cells.

EXPERIMENTAL SECTION

Synthesis. $Li_{6.4}La_3Zr_{1.4}Ta_{0.6}O_{12}$ (LLZTO) was purchased from MTI Corporation (μ_d = 5 μm) and pelletized in a 13 mm stainless steel die (Across International) at 2 t of pressure using a mechanical press (Carver model M). The resulting pellets were placed in MgO boats within a tube furnace (Thermcraft XST-3-0-36-1V2-F01) for a two-step sintering process,[34] which has been shown to help densify pellets while limiting lithium loss through an initial high-temperature (HT) nucleation step and then lower temperature grain growth. Pellets were initially heated to 1200 °C at a ramp rate of 3 °C/min and held for 1 h. The temperature was then reduced to 1100 °C and held for 5 h before cooling to room temperature at a rate of 100 °C/h. MgO boats were used to eliminate the effect of crucible doping, and the resulting pellets (Figure S1) showed no signs of contamination (Figure S2) by Mg from the boat.[35] X-ray diffraction (XRD) data for the sintered pellets agreed with the theoretical LLZTO structure (Figure S3). The approximate density of the pellets was 90 ± 4% (volume calculated with calipers). Faces of the pellets were polished in air progressively with 150, 220, 400, 800, and 1000 grit sandpapers (3M, proprietary ceramic), followed by wet polishing in ethanol with 1, 0.3, and 0.05 μm alumina particles (Electron Microscopy Sciences) to ensure a flat surface for electrode deposition as well as to reduce Li_2CO_3 contamination, and then immediately transferred into an argon-filled glovebox.[36] Pellets were transferred under argon to a radio frequency (RF)-sputtering deposition chamber built within an argon-filled glovebox (Angstrom Engineering), and LMO electrodes were deposited from a 2 in. LMO target (99.9% purity, ACI Alloys, Inc.). The sputter deposition was carried out at 60 W, 15 cm target distance, and 15 sccm argon flow. A stainless steel shadow mask with 10 mm diameter circles was used to control depositions on the LLZO pellets. Depositions were carried out for 2 h per electrode, with an estimated deposition rate of 0.9 nm/min. The thickness of sputtered films was estimated to be 110 nm by atomic force microscopy (AFM) (Figure S4). Further annealing was not performed due to prior evidence of reaction at ∼500 °C.[18] Gold current collectors were deposited using a three-boat thermal evaporator (CVC SC-3000) onto the sputtered films using the same mask.

The resulting LMO−LLZO pellets were transferred to a glovebox for cell assembly (MBRAUN Unilab Pro SP, O_2 <0.1 ppm, H_2O <0.5 ppm). For cells involving one or two lithium electrodes, lithium foils were punched (10 mm diameter), scraped to remove oxide, pressed onto the LLZO pellet, and placed into customized Swagelok cells (Figure S5). A spring inside the cell is compressed against the anodic current collector and then tightened via the compression fitting of the cell, yielding about 36 kPa pressure. The cells were then heated to 170 °C for at least 12 h[37] and then rescraped to remove any newly formed lithium oxide, which was recently shown to play a large role in the ability of the Li metal to wet LLZO.[38] The rescraping procedure was found to decrease the Li−LLZO interfacial impedance substantially and improve the resolution of other impedance features. Symmetric LMO cells were subjected to the same temperature treatment as Li-containing cells for consistency. All electrochemical testings occurred under the argon atmosphere in the same glovebox. A thermocouple was inserted into the Swagelok cells to monitor temperature for elevated temperature operation within an oven (Black and Decker; CF110—Across International). All electrochemical measurements were performed on a Bio-Logic SP-300 potentiostat/galvanostat/FRA.

Material Characterization. XRD data was obtained on a Bruker D2 Phaser. Scanning electron microscopy (SEM) images were taken using a JEOL JSM-7401F. XPS data was obtained on a Kratos AXIS Nova XPS system using a monochromated Al Kα source (1486.6 eV) and a pass energy of 160.0 eV. XPS binding energies were postcorrected based on Au, Ag, and Cu foil calibrations. Depth

https://dx.doi.org/10.1021/acsami.0c03519
ACS Appl. Mater. Interfaces 2020, 12, 24992−24999

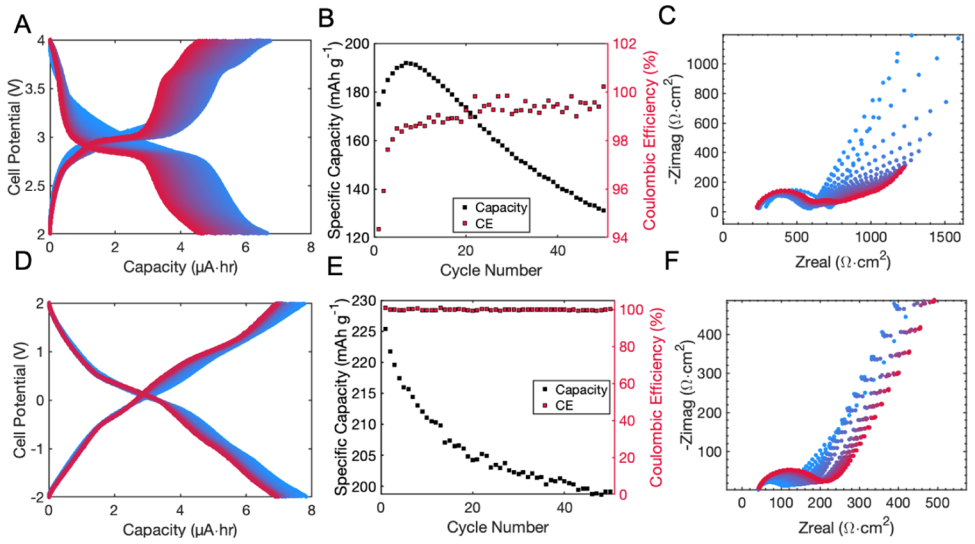

Figure 2. Polarization curves, discharge capacities, and Coulombic efficiencies and EIS evolution over 50 cycles at 100 °C for LMO|LLZO|Li cells (A–C) and LMO|LLZO|LMO cells (D–F). Blue curves represent the initial cycle, and transition toward red represents the 50th cycle. All cycling was performed at 3.8 μAh/cm^2 and is shown beginning on the charging phase after an initial discharge from 50% state of charge (SOC) (as synthesized).

profiling was carried out with Ar-ion milling with an incident energy of 3 keV.

Data Processing. EIS data was fit within MATLAB using equivalent circuit models and nonlinear least-squares regression. A detailed discussion of equivalent circuit determination and subsequent fitting can be found in the Supporting Information, and specific critical components are highlighted alongside the pertinent data in the Results and Discussion section.

RESULTS AND DISCUSSION

Cell Cycling. Before discussing the LMO–LLZO interface specifically, we first highlight the major features of polarization curves for the full, thin-film batteries using LMO as a cathode. LMO–LLZO–Li full cells were cycled galvanostatically between cell potentials from 2 to 4 V at both room temperature (RT, 23 ± 2 °C) and 100 °C (HT, 100 ± 2 °C). The voltage profiles, shown in Figures 2A (HT) and S6D (RT), were consistent with the sputter-deposited LMO, where the low crystallinity of the deposited films results in a continuous variation of cell voltage. This is in contrast to the behavior of crystalline LMO, which shows two well-defined voltage plateaus at roughly 2.9 and 4.0 V.[39,40] During initial cycles, HT cells accessed 172 ± 13.5 mAh/g (~64% of their theoretical capacity), shown in Figure 2B. In contrast, RT cells showed very low capacity (8.83 ± 6.01 mAh/g, ~3% of theoretical, Figure S6E). Here, theoretical capacities are estimated using the specific capacity of crystalline LMO (296 mAh/g), AFM-based estimates of the thickness (Figure S4), and the area of the electrodes. Thus, the estimates presented are conservative, as the films should exhibit lower density than bulk LMO. Over the subsequent course of 50 cycles, HT cells lost 25 ± 8.5% of their maximum capacity, while RT cells experienced negligible capacity fade. The low capacity of the RT cells is due to high cell impedance, dominated by the Li–LLZO interface. Briefly, we note that charge and discharge correspond to plating and stripping at the Li anode. During stripping, lithium metal voids have been shown to form at this interface, increasing the interfacial impedance (Figure 3).[41] Utilizing higher pressures and temperatures can better maintain and replenish interfacial contact,[14,42,43] but such effects are tangential to the current study of the LMO interface. It may also be noted that Li and LLZO have previously been shown to be kinetically stable against the reaction in the operating range of 0–5 V.[3–6]

To isolate features associated with the LMO–LLZO interface, symmetric cells were constructed with the architecture LMO|LLZO|LMO. Cycling of these LMO symmetric cells was performed within ±2 V (cell potential), which should approximately correspond to 2–4 V vs Li/Li$^+$. This range is approximate because both LMO electrodes shift in potential with charge passage, and the shifts are not identical above and below the open-circuit voltage (OCV). However, the range of 2–4 V is a fair point of reference as estimated by the similar capacities for the symmetric and full cells and the measured OCV of ~3 V (vs Li/Li$^+$) for the as-synthesized LMO in the full cell configuration. This voltage window corresponds to the lithium content approaching x = 0 within the accessible portion of $Li_xMn_2O_4$ at one electrode while approaching x = 2 at the opposing electrode and vice versa, thus making the theoretical symmetric cell capacity equivalent to the full cell capacity.

As shown in Figure 2D, symmetric LMO cells accessed up to 75% of their theoretical capacity (average initial specific capacity of 193 ± 22.8 mAh/g) at HT, while at RT, they accessed only ~7% (Figure S6B). Capacity fade was approximately 11% at HT and 1% at RT over 50 cycles (Figures 2D and S6B). The differences in accessible capacity between RT and HT cells are associated with a decrease in polarization resistance by roughly a factor of ~100 at elevated temperature, which can be seen in the Nyquist plots (Figures 2F and S6C). We found that HT cells could be cycled at a rate of >10C with a limited decrease to the accessed capacity, but for more direct comparison between temperatures, all cycling was carried out at C/3. Polarization curves for cycling at higher discharge rates can be found in Figure S7. EIS measurements of the symmetric LMO cells were repeated at the start of each half-cycle and did not substantially vary when compared at different depths of charge/discharge (see Figure S8). An increase in the overall cell impedance was observed with

https://dx.doi.org/10.1021/acsami.0c03519
ACS Appl. Mater. Interfaces 2020, 12, 24992–24999

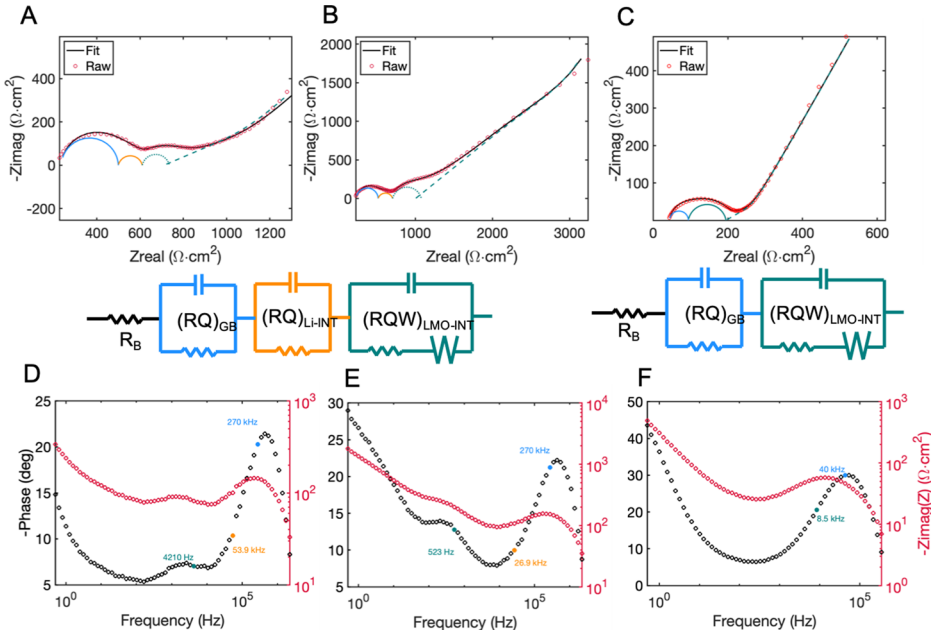

Figure 3. Nyquist plots (top), equivalent circuits (middle inset), and Bode plots (bottom) for LMO-containing cells tested at 100 °C in this study: (A) LMO|LLZO|Li postcharge, (B) LMO|LLZO|Li postdischarge, and (C) LMO|LLZO|LMO.

cycling for both the RT and HT symmetric cells (Figures 2F and S6C). The corresponding evolution of the impedance spectra is discussed in the following section in the context of the relevant physical conduction processes and equivalent circuit models.

Equivalent Circuit Modeling of Electrochemical Impedance Spectra. Equivalent circuit models for all cells and operating conditions were determined by a combination of phase inflection detection (PID) analysis,[44,45] characteristic time scale assessment, and comparison between full and symmetric cells with common components. Each circuit model comprises resistors (R) and constant phase elements (CPEs) (Q)—the parallel combination of which is generally attributed to one specific interfacial process and time constant—as well as generalized Warburg (W) elements to model diffusion-controlled processes. PID analysis utilizes changes in the slopes of impedance phase angle vs frequency (derivatives of the Bode plots) to aid in identifying distinct processes that merit an equivalent circuit component; inflection points in the phase angle become maxima or minima in the derivative and are more easily detected than corresponding features in the imaginary component of impedance. For our electrolyte and electrode dimensions (area = 0.79 cm^2; A/L = 7.9 cm), documented capacitance values for bulk, grain boundary, and interface impedances should generally be on the order of $\sim 10^{-11}$, $\sim 10^{-10}$–10^{-7}, and $\sim 10^{-7}$–10^{-5} F, respectively.[46] These estimates are used throughout the proceeding discussion to support the assignment of the individual circuit elements. Additional details regarding the elements, their functional forms, and additional analysis procedures performed during fitting are given in the Supporting Information.

An initial comparison among LMO symmetric, Li symmetric, and LMO–Li full cells permits identification of several EIS features that appear on differing time scales. Inspection of the Nyquist diagrams (Figures 3A–C and S9B) shows the presence of distinct (though depressed) semicircle features associated with each symmetric cell, both of which are resolvable in the spectra of the full cell. Warburg (diffusional) tailing is also clear in the low-frequency regime of both the symmetric LMO and full cells, indicating that it must arise from diffusion in LMO. However, to more definitively make equivalent circuit assignments, we also constructed ion-blocking cells (Au|LLZO|Au) to afford insight into the (intragranular) bulk and grain-boundary impedance of the electrolyte, which could in principle overlap high-frequency processes associated with the primary electrode materials. The Au symmetric EIS studies revealed two RC processes, as well as a capacitive effect due to the blocking electrodes, resulting in the equivalent circuit shown in Figure S9A. We attribute the higher-frequency process to the grain boundaries, consistent with its fit capacitance on the order of 10^{-7} F. The lower-frequency process (capacitance on the order of 10^{-4} F) has previously been observed at least once to our knowledge, although was not identified.[47] We suspect it is due to a slight alloying of lithium with gold, consistent with an increased resolution of the feature at high temperature and its fit capacitance value suggesting chemical reaction.[46]

Informed by the independent measurement of grain-boundary impedance, further interpretation of the symmetric Li, symmetric LMO, and LMO|LLZO|Li full cell EIS can be made. The semicircle noted in the Nyquist plots of LMO symmetric cells (Figure 3C) is highly depressed, which generally indicates the presence of multiple processes, rather than the alternative of an extremely nonideal capacitive feature (low CPE exponent).[48] Combined with the Warburg tailing at low frequency, these features were fit with RQ and RQW circuits, placed in series, to capture grain-boundary impedance and the electrode–electrolyte interface, respectively. The fitted capacitances of these elements were, respectively, on the order of 10^{-8} and 10^{-7} F. Due to the high fraction of theoretical capacity that was accessible at HT, the low-frequency diffusion was modeled by a finite-length Warburg open element (representing diffusion toward a reflective boundary), as is frequently invoked for intercalation materials.[49] Intercalation electrodes are known to exhibit diffusion that is linked to charge transfer, and thus the finite Warburg element is placed

https://dx.doi.org/10.1021/acsami.0c03519
ACS Appl. Mater. Interfaces 2020, 12, 24992–24999

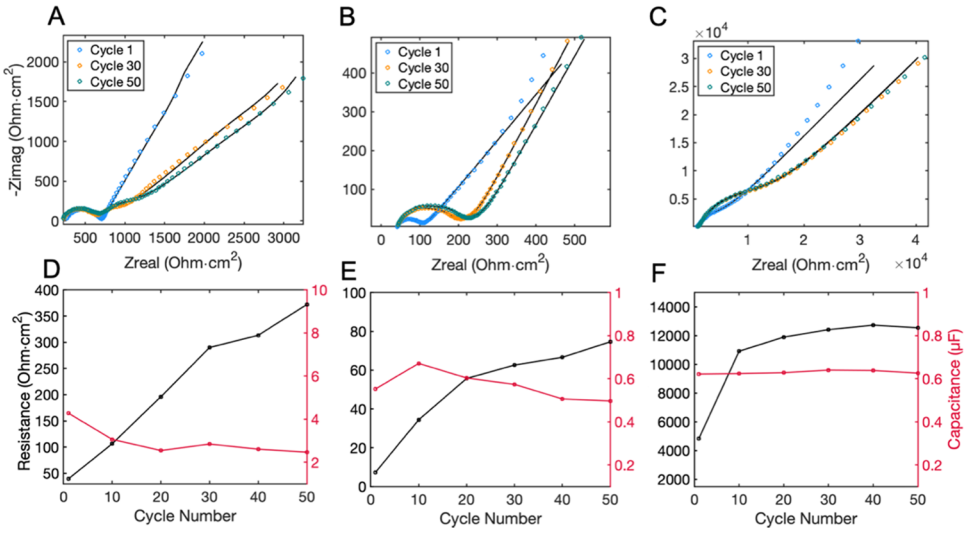

Figure 4. EIS and fits of full cells postdischarge at 100 °C (A) and LMO symmetric cells at HT (B) and RT (C). The respective resistances and capacitances assigned to the LMO−LLZO interface are plotted as a function of cycle number (D−F).

in series with the resistance while parallel to the capacitance for the best physical correspondence.[45] The same essential process and circuit were also used to fit the EIS from RT LMO symmetric cells, except that the finite Warburg element at HT was replaced by a standard Warburg element at RT, where much higher diffusion resistance effectively creates a semi-infinite boundary condition. Further specifics related to the Warburg impedance functions are discussed in the Supporting Information.

To compare cycle-dependent EIS of the Li−LLZO interface, lithium symmetric cells were cycled at 7.6 μA/cm^2 for 1 h, to 6 μA h capacity in each direction, to best approximate capacities relevant for the Li−LLZO interface in full cells at HT. EIS measurements were performed at the end of each half-cycle. The impedance response (Figure S9B) showed a primary, depressed Nyquist semicircle attributable to the series impedance of grain boundaries and the Li−LLZO interface, which exhibit reasonable fit capacitance values of 10^{-8} and 10^{-6} F (equivalent circuit in Figure S9B).

Equipped with equivalent circuit information for the bulk materials and both interfaces, the full cell EIS could then be evaluated. The highest-frequency, stretched semicircle of the full cell impedance spectra (Figure 3A) was assigned to the combination of grain boundaries and the Li−LLZO interface, in accordance with their fit capacitance values of 10^{-9} and 10^{-7} F, respectively. The second semicircle and subsequent diffusional (Warburg open) response were attributed to the LMO−LLZO interface likewise through the value and agreement of the fit capacitance (10^{-6}−10^{-7} F) with the symmetric cell data. Fitting of the EIS of the full cells at room temperature mirrored the above procedure for the high-temperature data. However, because the impedance of the full cells was found to be dominated by the Li interface at lower temperatures, the fitting does not provide insight into the LMO−LLZO interface under these conditions. Increasing the stack pressure of future cells may resolve this difficulty and permit interpretation at lower temperatures.[42,43]

Having constructed the overall equivalent circuit diagrams, the LMO full cells and LMO symmetric cells were fitted iteratively over the course of cycling to track the evolution of the cell components. Figure 3A−C shows representative impedance spectra for a discharged full cell (charged cell shown in Figure S10), as well as for symmetric cells at both RT and HT. Below these (Figure 4D−F) are shown the tracked values of the resistance and capacitance associated with the LMO−LLZO interface in each cell; complete sets of circuit element parameter values for each model are presented in Tables S2−S6 in the Supporting Information. The difference in magnitude of interfacial resistances between the HT and RT cells is due to a reduction of this resistance with increasing temperature, while changes over time in each data set correspond to evolution within the cell. The primary quantifiable conclusion of these results is that the LMO−LLZO interfacial resistance (R_{CT}) increases steadily over time while the associated interfacial capacitance (Q_{CT}) stays relatively constant (Figure 4D−F). This is a critical observation because if an increase in resistance were due to a decrease in the contact area, one would expect a corresponding decrease in capacitance as well. Instead, the minor observed change in Q_{CT}, coupled with growth in R_{CT}, indicates that the interfacial area of the LMO electrodes remains relatively constant, suggesting that increases in the resistance are due to fundamental changes in the nature of the interface, such as the formation of a less-conductive interfacial decomposition product. This effect is present in cells cycled at both temperatures, although changes are much more pronounced and grow continuously in the HT cells.

XPS Depth Profiling. To further investigate the possibility of interfacial products between LMO and LLZO, we performed XPS depth profiling[21,23] on cells before and after cycling. We present the depth profiles by fractional signal contribution, defined as $I_A/(I_A + I_B)$, where I is the integrated XPS signal intensity, for elemental pairs. This metric illustrates changes to the relative quantity of each element spanning across the interface between each bulk phase. Figure 5 shows depth profiles for Mn, La, and Zr in the RT (A) and HT (B) cycled cells, overlaid on a control sample that was subjected to the same pretreatment (170 °C) as the cycled cells. To minimize possible artifacts from small differences in film thicknesses and etch rates, the profiles are aligned to the point at which the elemental signal contributions are equal. Changes in the spatial extent of an elemental signal must then be related

https://dx.doi.org/10.1021/acsami.0c03519
ACS Appl. Mater. Interfaces 2020, 12, 24992−24999

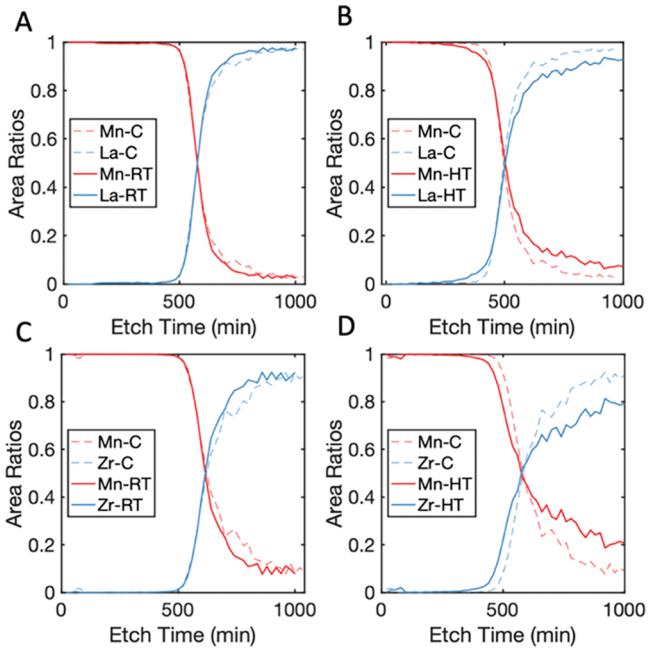

Figure 5. XPS depth profiles taken after cycling at RT (A, C) and HT (C, D), overlaid on uncycled control depth profiles for selected pairs of elements. Data is presented as fractional signal contribution among the elements compared. (A, B) Mn $2p_{3/2}$ vs La $3d_{5/2}$ and (C, D) Mn $2p_{3/2}$ vs Zr 3d.

to interdiffusion (barring large variance in interfacial roughness between samples). Consistency between control samples and the profiles of several apparently immobile elements gives an indication that interfacial roughness was reproducible and thus that changes to the spatial distributions can be attributed to element migration.

A clear difference in the interfacial composition profile is observed between the cell cycled at high temperature and the uncycled cell. The concentration profiles at elevated temperature specifically suggest migration of Mn atoms and thus the likely formation of a reaction zone penetrating into the electrolyte side of the interface. The RT cell experienced far less Mn diffusion, but this is not surprising due to both the inherently slower kinetics at low temperature and the significantly lower accessible capacity, which results in passage of much less total charge during cycling. Since cycling at high temperature results in a greater extent of interdiffusion than heat treatment alone (control sample), we hypothesize that the same decomposition behavior may be exhibited at low temperature over substantially longer cycling periods. The full elemental spectra for species profiled in Figure 5 are shown in Figure S11. However, due to well-documented complications of selective sputtering (inherent in all depth profiles), as well as evidence of sample charging, we do not assign a specific chemical state or phase to the reaction product(s) at this time.[50−52] Full composition profiles for all elements monitored (La, Mn, O, C, Zr, Li, Au) can be seen in Figure S12, and full spectra for C and Li regions can be seen in Figure S13.

It is noteworthy that in the full composition profiles, all samples show a spike in the concentration of oxygen at the interface (Figure S12). The feature could possibly relate to different metal oxide stoichiometries but could also relate to Li_2CO_3 contamination, which is a well-documented issue for LLZO upon any brief atmospheric exposure.[23,53,54] The carbon signal was tracked for these samples as well and did reveal the possible presence of Li_2CO_3, though there was not a clear correlation between C and O signals. Thus, while better polishing and handling protocols could be implemented to further reduce such sources of ambiguity, the present data are still consistent with a reaction between the electrode and electrolyte metal oxides.

Regarding the possible identity of products, precise phase identification is a challenge at buried interfaces, and even more powerful X-ray absorption techniques can be left with ambiguities in assignments.[23] Nonetheless, computational studies have suggested possible products for a reaction between LLZO and the cathode material $LiMnO_2$, closely related to LMO ($LiMn_2O_4$).[16] Depending on the voltage, several binary metal oxides, lithiated manganese-deficient oxides, $La_xZr_yO_z$ compounds, and $LaMn_2O_5$ have been predicted as possible reaction products. The formation of a Mn-deficient Mn-oxide phase or a La−Mn mixed metal oxide would be most consistent with the observation of Mn migration into the electrolyte region.

CONCLUSIONS

Thin-film LMO electrodes were used to investigate the LMO−LLZO interface and its stability during electrochemical operation. The combination of ion-blocking electrodes, symmetric cells, and full cells permitted isolation of individual cell interfaces and identification of key EIS signatures. Battery operation resulted in an apparent cycling-induced reaction between LMO and LLZO. EIS data from full and symmetric cell cycling indicated that this product increased the interfacial impedance of the cell, contributing to the capacity fade. XPS further showed that changes at the interface were associated with the formation of a reaction zone. Specifically, Mn was detected across the interfacial region, which widened after cycling at higher temperatures, suggesting the migration of these atoms from the cathode into the LLZO. We note that the amorphous nature of the films may make them more prone to reaction than crystalline LMO but that the present findings still place a conservative boundary on these materials' compatibility.

Irrespective of the growth of the interfacial product, the initial impedance of the LMO−LLZO interface was larger than desirable for a commercial battery. While extensive polishing was used to reduce Li_2CO_3 contamination, it was still detected via XPS, and further reduction of interfacial contaminants may help to reduce this impedance. Additional methods to passivate and reduce the impedance of the interface, such as the addition of interlayers, could be investigated and subjected to the same analysis to assess interfacial degradation in future work. Along these lines, one recent study used a $Li_{2.3}C_{0.7}B_{0.3}O_3$ interlayer to lower interfacial impedance against LLZO, though capacity fade was later seen due to mechanical degradation.[55] Computational studies have also looked at the stability of a large range of possible interlayer materials, with $LiGaO_2$ and $LiNbO_3$[56] as well as Li_2ZrO_3[57] identified for high chemical compatibility as SSE interlayers. Experimental verification of the stability of these possible interlayers is still necessary, and one such way to better understand their effect would be the construction of a series of symmetric and full cells, as was done in this study, to allow the effects of these interlayers to be isolated and probed. The methodology presented here serves as a useful template for further study of solid-state electrochemical interfaces.

https://dx.doi.org/10.1021/acsami.0c03519
ACS Appl. Mater. Interfaces 2020, 12, 24992−24999

■ ASSOCIATED CONTENT

Supporting Information

The Supporting Information is available free of charge at https://pubs.acs.org/doi/10.1021/acsami.0c03519.

Optical and SEM images of cells; full polarization curves and EIS for room temperature cycling and for cycling at a variable rate; XPS survey spectra (postsynthesis and polishing) as well as focus regions of La, Mn, Zr, Li, O, and C during depth profiling; XRD of LLZO pellets before and after LMO deposition; EIS fitting discussion and tables of fit parameters (PDF)

■ AUTHOR INFORMATION

Corresponding Author

Adam Holewinski − *Department of Chemical and Biological Engineering, Renewable and Sustainable Energy Institute, and Materials Science and Engineering Program, University of Colorado, Boulder, Colorado 80309, United States;* orcid.org/0000-0001-8307-5881; Email: adam.holewinski@colorado.edu

Authors

Alexander A. Delluva − *Department of Chemical and Biological Engineering and Renewable and Sustainable Energy Institute, University of Colorado, Boulder, Colorado 80309, United States*

Jessica Dudoff − *Renewable and Sustainable Energy Institute and Materials Science and Engineering Program, University of Colorado, Boulder, Colorado 80309, United States*

Glenn Teeter − *National Renewable Energy Laboratory, Golden, Colorado 80401, United States*

Complete contact information is available at: https://pubs.acs.org/10.1021/acsami.0c03519

Notes

The authors declare no competing financial interest.

■ ACKNOWLEDGMENTS

This work was funded by NSF CBET #1806059. The COSINC-CHR and COSINC-FAB facilities at CU Boulder were utilized for some synthesis and characterization. The authors acknowledge Drs. Yun Xu and Chaiwait Engtrakul and the National Renewable Energy Lab for their assistance in the synthesis of the LMO cathodes, Adrienne Blevins for assistance with the AFM measurements, and Dragan Mejic for assistance in creating the Swagelok cells.

■ REFERENCES

(1) Luntz, A. C.; Voss, J.; Reuter, K. Interfacial Challenges in Solid-State Li Ion Batteries. *J. Phys. Chem. Lett.* **2015**, *6*, 4599−4604.

(2) Wu, B.; Wang, S.; Evans, W. J., IV; Deng, D. Z.; Yang, J.; Xiao, J. Interfacial Behaviours between Lithium Ion Conductors and Electrode Materials in Various Battery Systems. *J. Mater. Chem. A* **2016**, *4*, 15266−15280.

(3) Kotobuki, M.; Kanamura, K.; Sato, Y.; Yoshida, T. Fabrication of All-Solid-State Lithium Battery with Lithium Metal Anode Using Al_2O_3-Added $Li_7La_3Zr_2O_{12}$ Solid Electrolyte. *J. Power Sources* **2011**, *196*, 7750−7754.

(4) Thompson, T.; Yu, S.; Williams, L.; Schmidt, R. D.; Garcia-Mendez, R.; Wolfenstine, J.; Allen, J. L.; Kioupakis, E.; Siegel, D. J.; Sakamoto, J. Electrochemical Window of the Li-Ion Solid Electrolyte $Li_7La_3Zr_2O_{12}$. *ACS Energy Lett.* **2017**, *2*, 462−468.

(5) Nakayama, M.; Kotobuki, M.; Munakata, H.; Nogami, M.; Kanamura, K. First-Principles Density Functional Calculation of Electrochemical Stability of Fast Li Ion Conducting Garnet-Type Oxides. *Phys. Chem. Chem. Phys.* **2012**, *14*, 10008−10014.

(6) Ma, C.; Cheng, Y.; Yin, K.; Luo, J.; Sharafi, A.; Sakamoto, J.; Li, J.; More, K. L.; Dudney, N. J.; Chi, M. Interfacial Stability of Li Metal-Solid Electrolyte Elucidated via in Situ Electron Microscopy. *Nano Lett.* **2016**, *16*, 7030−7036.

(7) Zhu, Y.; Connell, J. G.; Tepavcevic, S.; Zapol, P.; Garcia-Mendez, R.; Taylor, N. J.; Sakamoto, J.; Ingram, B. J.; Curtiss, L. A.; Freeland, J. W.; et al. Dopant-Dependent Stability of Garnet Solid Electrolyte Interfaces with Lithium Metal. *Adv. Energy Mater.* **2019**, *9*, No. 1803440.

(8) Sharafi, A.; Kazyak, E.; Davis, A. L.; Yu, S.; Thompson, T.; Siegel, D. J.; Dasgupta, N. P.; Sakamoto, J. Surface Chemistry Mechanism of Ultra-Low Interfacial Resistance in the Solid-State Electrolyte $Li_7La_3Zr_2O_{12}$. *Chem. Mater.* **2017**, *29*, 7961−7968.

(9) Han, F.; Westover, A. S.; Yue, J.; Fan, X.; Wang, F.; Chi, M.; Leonard, D. N.; Dudney, N. J.; Wang, H.; Wang, C. High Electronic Conductivity as the Origin of Lithium Dendrite Formation within Solid Electrolytes. *Nat. Energy* **2019**, *4*, 187−196.

(10) Swamy, T.; Park, R.; Sheldon, B. W.; Rettenwander, D.; Porz, L.; Berendts, S.; Uecker, R.; Craig Carter, W.; Chiang, Y. M. Lithium Metal Penetration Induced by Electrodeposition through Solid Electrolytes: Example in Single-Crystal $Li_6La_3ZrTaO_{12}$ Garnet. *J. Electrochem. Soc.* **2018**, *165*, A3648−A3655.

(11) Porz, L.; Swamy, T.; Sheldon, B. W.; Rettenwander, D.; Frömling, T.; Thaman, H. L.; Berendts, S.; Uecker, R.; Carter, W. C.; Chiang, Y. M. Mechanism of Lithium Metal Penetration through Inorganic Solid Electrolytes. *Adv. Energy Mater.* **2017**, *7*, No. 1701003.

(12) Taylor, N. J.; Stangeland-Molo, S.; Haslam, C. G.; Sharafi, A.; Thompson, T.; Wang, M.; Garcia-Mendez, R.; Sakamoto, J. Demonstration of High Current Densities and Extended Cycling in the Garnet $Li_7La_3Zr_2O_{12}$ solid Electrolyte. *J. Power Sources* **2018**, *396*, 314−318.

(13) Albertus, P.; Babinec, S.; Litzelman, S.; Newman, A. Status and Challenges in Enabling the Lithium Metal Electrode for High-Energy and Low-Cost Rechargeable Batteries. *Nat. Energy* **2018**, *3*, 16−21.

(14) Krauskopf, T.; Hartmann, H.; Zeier, W. G.; Janek, J. Toward a Fundamental Understanding of the Lithium Metal Anode in Solid-State Batteries - An Electrochemo-Mechanical Study on the Garnet-Type Solid Electrolyte $Li_{6.25}Al_{0.25}La_3Zr_2O_{12}$. *ACS Appl. Mater. Interfaces* **2019**, *11*, 14463−14477.

(15) Il'ina, E. A.; Raskovalov, A. A. Studying of Superionic Solid Electrolyte $Li_7La_3Zr_2O_{12}$ Stability by Means of Chemical Thermodynamics for Application in All-Solid-State Batteries. *Electrochim. Acta* **2020**, *330*, No. 135220.

(16) Miara, L. J.; Richards, W. D.; Wang, Y. E.; Ceder, G. First-Principles Studies on Cation Dopants and Electrolyte|Cathode Interphases for Lithium Garnets. *Chem. Mater.* **2015**, *27*, 4040−4047.

(17) Wakasugi, J.; Munakata, H.; Kanamura, K. Thermal Stability of Various Cathode Materials against $Li_{6.25}Al_{0.25}La_3Zr_2O_{12}$ Electrolyte. *Electrochemistry* **2017**, *85*, 77−81.

(18) Ren, Y.; Liu, T.; Shen, Y.; Lin, Y.; Nan, C. W. Chemical Compatibility between Garnet-like Solid State Electrolyte $Li_{6.75}La_3Zr_{1.75}Ta_{0.25}O_{12}$ and Major Commercial Lithium Battery Cathode Materials. *J. Materiomics* **2016**, *2*, 256−264.

(19) Park, K.; Yu, B. C.; Jung, J. W.; Li, Y.; Zhou, W.; Gao, H.; Son, S.; Goodenough, J. B. Electrochemical Nature of the Cathode Interface for a Solid-State Lithium-Ion Battery: Interface between $LiCoO_2$ and Garnet-$Li_7La_3Zr_2O_{12}$. *Chem. Mater.* **2016**, *28*, 8051−8059.

(20) Ohta, S.; Kobayashi, T.; Seki, J.; Asaoka, T. Electrochemical Performance of an All-Solid-State Lithium Ion Battery with Garnet-Type Oxide Electrolyte. *J. Power Sources* **2012**, *202*, 332−335.

(21) Zarabian, M.; Bartolini, M.; Pereira-Almao, P.; Thangadurai, V. X-Ray Photoelectron Spectroscopy and AC Impedance Spectroscopy Studies of Li-La-Zr-O Solid Electrolyte Thin Film/$LiCoO_2$ Cathode Interface for All-Solid-State Li Batteries. *J. Electrochem. Soc.* **2017**, *164*, A1133−A1139.

(22) Tsai, C. L.; Ma, Q.; Dellen, C.; Lobe, S.; Vondahlen, F.; Windmüller, A.; Grüner, D.; Zheng, H.; Uhlenbruck, S.; Finsterbusch, M.; et al. A Garnet Structure-Based All-Solid-State Li Battery without Interface Modification: Resolving Incompatibility Issues on Positive Electrodes. *Sustainable Energy Fuels* **2019**, *3*, 280−291.
(23) Vardar, G.; Bowman, W. J.; Lu, Q.; Wang, J.; Chater, R. J.; Aguadero, A.; Seibert, R.; Terry, J.; Hunt, A.; Waluyo, I.; et al. Structure, Chemistry, and Charge Transfer Resistance of the Interface between $Li_7La_3Zr_2O_{12}$ Electrolyte and $LiCoO_2$ Cathode. *Chem. Mater.* **2018**, *30*, 6259−6276.
(24) Yan, X.; Li, Z.; Wen, Z.; Han, W. Li/$Li_7La_3Zr_2O_{12}$/$LiFePO_4$all-Solid-State Battery with Ultrathin Nanoscale Solid Electrolyte. *J. Phys. Chem. C* **2017**, *121*, 1431−1435.
(25) Hänsel, C.; Afyon, S.; Rupp, J. L. M. Investigating the All-Solid-State Batteries Based on Lithium Garnets and a High Potential Cathode-$LiMn_{1.5}Ni_{0.5}O_4$. *Nanoscale* **2016**, *8*, 18412−18420.
(26) Zhang, N.; Long, X.; Wang, Z.; Yu, P.; Han, F.; Fu, J.; Ren, G.; Wu, Y.; Zheng, S.; Huang, W.; et al. Mechanism Study on the Interfacial Stability of a Lithium Garnet-Type Oxide Electrolyte against Cathode Materials. *ACS Appl. Energy Mater.* **2018**, *1*, 5968−5976.
(27) Wang, D.; Sun, Q.; Luo, J.; Liang, J.; Sun, Y.; Li, R.; Adair, K.; Zhang, L.; Yang, R.; Lu, S.; et al. Mitigating the Interfacial Degradation in Cathodes for High-Performance Oxide-Based Solid-State Lithium Batteries. *ACS Appl. Mater. Interfaces* **2019**, *11*, 4954−4961.
(28) Jin, Y.; McGinn, P. J. Al-Doped $Li_7La_3Zr_2O_{12}$ Synthesized by a Polymerized Complex Method. *J. Power Sources* **2011**, *196*, 8683−8687.
(29) Put, B.; Vereecken, P. M.; Labyedh, N.; Sepulveda, A.; Huyghebaert, C.; Radu, I. P.; Stesmans, A. High Cycling Stability and Extreme Rate Performance in Nanoscaled $LiMn_2O_4$ Thin Films. *ACS Appl. Mater. Interfaces* **2015**, *7*, 22413−22420.
(30) Fehse, M.; Trócoli, R.; Ventosa, E.; Hernández, E.; Sepúlveda, A.; Morata, A.; Tarancón, A. Ultrafast Dischargeable $LiMn_2O_4$ Thin-Film Electrodes with Pseudocapacitive Properties for Microbatteries. *ACS Appl. Mater. Interfaces* **2017**, *9*, 5295−5301.
(31) Dudney, N. J. Solid-State Thin-Film Rechargeable Batteries. *Mater. Sci. Eng., B* **2005**, *116*, 245−249.
(32) Dudney, N. J.; Bates, J. B.; Zuhr, R. A.; Young, S.; Robertson, J. D.; Jun, H. P.; Hackney, S. A. Nanocrystalline $Li_xMn_{2-y}O_4$ Cathodes for Solid-State Thin-Film Rechargeable Lithium Batteries. *J. Electrochem. Soc.* **2000**, 2455−2464.
(33) Iriyama, Y.; Nishimoto, K.; Yada, C.; Abe, T.; Ogumi, Z.; Kikuchi, K. Charge-Transfer Reaction at the Lithium Phosphorus Oxynitride Glass Electrolyte/Lithium Manganese Oxide Thin-Film Interface and Its Stability on Cycling. *J. Electrochem. Soc.* **2006**, *153*, A821.
(34) Huang, X.; Xiu, T.; Badding, M. E.; Wen, Z. Two-Step Sintering Strategy to Prepare Dense Li-Garnet Electrolyte Ceramics with High Li+ Conductivity. *Ceram. Int.* **2017**, 5660.
(35) Matsui, M.; Takahashi, K.; Sakamoto, K.; Hirano, A.; Takeda, Y.; Yamamoto, O.; Imanishi, N. Phase Stability of a Garnet-Type Lithium Ion Conductor $Li_7La_3Zr_2O_{12}$. *Dalton Trans.* **2014**, *43*, 1019−1024.
(36) Sharafi, A.; Yu, S.; Naguib, M.; Lee, M.; Ma, C.; Meyer, H. M.; Nanda, J.; Chi, M.; Siegel, D. J.; Sakamoto, J. Impact of Air Exposure and Surface Chemistry on Li−$Li_7La_3Zr_2O_{12}$ Interfacial Resistance. *J. Mater. Chem. A* **2017**, *5*, 13475−13487.
(37) Sharafi, A.; Meyer, H. M.; Nanda, J.; Wolfenstine, J.; Sakamoto, J. Characterizing the Li-$Li_7La_3Zr_2O_{12}$ Interface Stability and Kinetics as a Function of Temperature and Current Density. *J. Power Sources* **2016**, *302*, 135−139.
(38) Zheng, H.; Wu, S.; Tian, R.; Xu, Z.; Zhu, H.; Duan, H.; Liu, H. Intrinsic Lithiophilicity of Li−Garnet Electrolytes Enabling High-Rate Lithium Cycling. *Adv. Funct. Mater.* **2019**, No. 1906189.
(39) Liu, C.; Neale, Z. G.; Cao, G. Understanding Electrochemical Potentials of Cathode Materials in Rechargeable Batteries. *Mater. Today* **2016**, *19*, 109−123.
(40) Bates, J. B.; Dudney, N. J.; Lubben, D. C.; Gruzalski, G. R.; Kwak, B. S.; Yu, X.; Zuhr, R. A. Thin-Film Rechargeable Lithium Batteries. *J. Power Sources* **1995**, *54*, 58−62.
(41) Koshikawa, H.; Matsuda, S.; Kamiya, K.; Miyayama, M.; Kubo, Y.; Uosaki, K.; Hashimoto, K.; Nakanishi, S. Dynamic Changes in Charge-Transfer Resistance at Li Metal/$Li_7La_3Zr_2O_{12}$ interfaces during Electrochemical Li Dissolution/Deposition Cycles. *J. Power Sources* **2018**, *376*, 147−151.
(42) Wang, M. J.; Choudhury, R.; Sakamoto, J. Characterizing the Li-Solid-Electrolyte Interface Dynamics as a Function of Stack Pressure and Current Density. *Joule* **2019**, *3*, 2165−2178.
(43) Krauskopf, T.; Mogwitz, B.; Rosenbach, C.; Zeier, W. G.; Janek, J. Diffusion Limitation of Lithium Metal and Li−Mg Alloy Anodes on LLZO Type Solid Electrolytes as a Function of Temperature and Pressure. *Adv. Energy Mater.* **2019**, No. 1902568.
(44) Cassel, A.; Fleutot, B.; Courty, M.; Viallet, V.; Morcrette, M. Sol-Gel Synthesis and Electrochemical Properties Extracted by Phase Inflection Detection Method of NASICON-Type Solid Electrolytes $LiZr_2(PO_4)_3$ and $Li_{1.2}Zr_{1.9}Ca_{0.1}(PO_4)_3$. *Solid State Ionics* **2017**, *309*, 63−70.
(45) Larfaillou, S.; Guy-Bouyssou, D.; Le Cras, F.; Franger, S. Comprehensive Characterization of All-Solid-State Thin Films Commercial Microbatteries by Electrochemical Impedance Spectroscopy. *J. Power Sources* **2016**, *319*, 139−146.
(46) West, A.; Irvine, J.; Sinclair, D. Electroceramics: Characterization by Impedance Spectroscopy. *Adv. Mater.* **1990**, *2*, 132−138.
(47) Tenhaeff, W. E.; Rangasamy, E.; Wang, Y.; Sokolov, A. P.; Wolfenstine, J.; Sakamoto, J.; Dudney, N. J. Resolving the Grain Boundary and Lattice Impedance of Hot-Pressed $Li_7La_3Zr_2O_{12}$ Garnet Electrolytes. *ChemElectroChem* **2014**, *1*, 375−378.
(48) Orazem, M. E.; Pâbre, N.; Tribollet, B. Enhanced Graphical Representation of Electrochemical Impedance Data. *J. Electrochem. Soc.* **2006**, *153*, B129−B136.
(49) Lim, C., IV *Transport Phenomena. Lecture 20: Warburg Impedance*; MIT OpenCourseWare, 1899; pp 1−7.
(50) Malherbe, J. B.; Hofmann, S.; Sanz, J. M. Preferential Sputtering of Oxides: A Comparison of Model Predictions with Experimental Data. *Appl. Surf. Sci.* **1986**, *27*, 355−365.
(51) Lobe, S.; Dellen, C.; Windmüller, A.; Tsai, C. L.; Vondahlen, F.; Uhlenbruck, S.; Guillon, O. Challenges Regarding Thin Film Deposition of Garnet Electrolytes for All-Solid-State Lithium Batteries with High Energy Density. *Ionics* **2018**, *24*, 2199−2208.
(52) Wood, K. N.; Teeter, G. XPS on Li Battery Related Compounds: Analysis of Inorganic SEI Phases and a Methodology for Charge Correction. *ACS Appl. Energy Mater.* **2018**, *1*, 4493.
(53) Cheng, L.; Crumlin, E. J.; Chen, W.; Qiao, R.; Hou, H.; Franz Lux, S.; Zorba, V.; Russo, R.; Kostecki, R.; Liu, Z.; et al. The Origin of High Electrolyte-Electrode Interfacial Resistances in Lithium Cells Containing Garnet Type Solid Electrolytes. *Phys. Chem. Chem. Phys.* **2014**, *16*, 18294−18300.
(54) Cheng, L.; Liu, M.; Mehta, A.; Xin, H.; Lin, F.; Persson, K.; Chen, G.; Crumlin, E. J.; Doeff, M. Garnet Electrolyte Surface Degradation and Recovery. *ACS Appl. Energy Mater.* **2018**, *1*, 7244−7252.
(55) Han, F.; Yue, J.; Chen, C.; Zhao, N.; Fan, X.; Ma, Z.; Gao, T.; Wang, F.; Guo, X.; Wang, C. Interphase Engineering Enabled All-Ceramic Lithium Battery. *Joule* **2018**, *2*, 497−508.
(56) Yu, S.; Park, H.; Siegel, D. J. Thermodynamic Assessment of Coating Materials for Solid-State Li, Na, and K Batteries. *ACS Appl. Mater. Interfaces* **2019**, *11*, 36607−36615.
(57) Xiao, Y.; Miara, L. J.; Wang, Y.; Ceder, G. Computational Screening of Cathode Coatings for Solid-State Batteries. *Joule* **2019**, *3*, 1252−1275.

NOTE ADDED AFTER ASAP PUBLICATION

This paper was published on the Web on May 18, 2020, with axes errors in Figure 3, and S9 in the Supporting Information. The corrected versions were reposted on May 19, 2020.

https://dx.doi.org/10.1021/acsami.0c03519
ACS Appl. Mater. Interfaces 2020, 12, 24992−24999